

Late-Type Dwarf Galaxies in the Virgo Cluster: I. The Samples

Elchanan Almoznino* Noah Brosch

*Wise Observatory & School of Physics and Astronomy,
Raymond and Beverly Sackler Faculty of Exact Sciences,
Tel-Aviv University*

Abstract

We selected complete samples of late-type dwarf galaxies in the Virgo cluster with HI information. The galaxies were observed at the Wise-Observatory using several broad-band and H α bandpasses. UV measurements were carried out with the IUE Observatory from VILSPA, and use was made of images from the FAUST shuttle-borne UV telescope.

We describe our observations in detail, paying particular attention to the determination of measurement errors, and present the observational results together with published data and far-infrared information from IRAS. The sample will be analyzed in subsequent papers, in order to study star formation mechanisms.

Key words: Galaxies, star-formation; Galaxies, evolution; Galaxies, individual

1 Introduction

The process of star formation is probably the most fundamental process in galactic evolution, and it has various implications on global, as well as local phenomena. In all galaxies, the star formation is initiated by the gravitational collapse of gas clouds, followed by fragmentation into future individual stars. When stars enter the main sequence, the radiation pressure and stellar winds push on the ambient gas and prevent it from further collapsing. Eventually, only a small fraction of the cloud mass is converted into stars.

*email - nan@wise.tau.ac.il

The star formation process is characterized by two main parameters: the initial mass function (IMF) and the total star formation rate (SFR). First introduced by Salpeter in 1955, the IMF is usually described as a power law in the range of 2–2.5, while the original value proposed by Salpeter is 2.35. Other characteristics of the IMF are the low and high mass limits, usually taken as $0.1M_{\odot}$ and $60\text{--}120M_{\odot}$.

As for the SFR, its time dependence varies dramatically between different galactic types (e.g., Gallagher, Hunter and Tutukov 1984, Kennicutt *et al.* 1994). In early type galaxies, the star formation usually decays smoothly with time. In late-type galaxies, on the other hand, the star formation is generally more intense, and the SFR is subject to significant changes within short timescales. Some galaxies experience bursts of star formation in which the SFR may be higher by more than an order of magnitude than during their quiescent epochs.

Despite extensive progress in understanding the star formation process, there are several issues still not fully understood, due to the complexity of this process. One can summarize the currently open issues, concerning the star formation processes in galaxies, in two major questions: (1) What are the mechanisms that govern the star formation process, and how do they depend on the galactic type and environment? (2) How do the SFR and IMF depend on various galactic properties, such as interstellar gas density, morphology of the interstellar gas, metallicity, and the amount of dust in the interstellar medium.

A simplified assumption is that the SFR depends directly on the density of the interstellar gas (Schmidt law: Schmidt 1959). Actually, the observable quantity is the gas surface density. Testing this parameter against the SFR in normal galaxies indicates that there is a threshold gas surface density, below which no star formation takes place (Kennicutt 1989). The value of this threshold surface density varies from galaxy to galaxy, thus it is not a global parameter, though it is believed to be of order a few times $10^{20} \text{ atoms/cm}^2$.

In order to find the SFR in a sample of galaxies, one needs to know the IMF that describes the star formation in these galaxies. The IMF can be found by fitting a number of observed properties, such as broad-band colors, to a set of models of different stellar populations, with different IMFs (population synthesis). By comparing the various color indices to the synthetic colors calculated from models one can, in principle, determine the IMF of the galaxies in the sample. This requires a database spanning as large a range in wavelengths as possible to eliminate the degeneracy of results in several conditions, namely, to be able to distinguish between different conditions that yield the same value for one or more colors. It is important that one of the measured bands is in the UV regime, in order to trace the massive stars which contribute most of the energy emitted in this part of the spectrum.

The few observational methods for measuring the SFR make use of the direct or indirect contribution of massive stars to the observed properties of the galaxies. The most direct observational trace of massive stars (in galaxies in which individual stars cannot be resolved and investigated) is their UV emission. The more massive the

star, the more intense its UV radiation and the shorter the wavelength of its peak emission.

The major disadvantage of this method is the heavy extinction by dust in the UV. This is very difficult to estimate, mainly because the spatial distribution of dust in a galaxy affects its apparent optical depth as derived from the optical domain. Any estimate of the extinction in the UV using optical extinction and a standard extinction law may lead to large errors due to this effect. One may use the far IR emission from the dust to measure the UV flux responsible for its heating, but again, due to differences in spatial dust distribution and in dust properties the result will be inaccurate.

It should be noted that the UV radiation discussed here is at longer wavelengths than the Lyman break (912\AA). This is because ionizing photons are immediately absorbed by the interstellar gas and cannot be observed directly or through their influence on the surrounding dust. The absorption of the Lyman continuum (LyC) photons by hydrogen gives rise to a number of phenomena, which can be used to measure indirectly the number of LyC photons emitted by the newly formed stars, and hence to determine the current high mass ($M > 10\text{--}15 M_{\odot}$) SFR. As explained above, this implies that we can trace the very massive stars but our result would suffer from errors induced by the uncertainties in the IMF.

The LyC photons ionize hydrogen gas, producing essentially one free electron per each LyC photon (Case B recombination theory). The intensity of these lines can be calculated using a Case B recombination model (Osterbrock 1989). The Balmer lines' intensity scales directly with the LyC flux and, in general, it depends weakly also on the gas temperature and density. Another difficulty arises from the assumption of Case B. It is believed that the majority of the LyC photons are absorbed by the hydrogen, but some may be lost to dust or may escape from the HII region. This effect is believed to be small, and will be discussed later. In general, the determination of the SFR using hydrogen line intensities is robust.

One of the most common methods, adopted also here, makes use of the $H\alpha$ line. The $H\alpha$ line has been used by many (Kennicutt 1983, Kennicutt and Kent 1983, Gallagher, Hunter and Tutukov 1984, Pogge and Eskridge 1987, Kennicutt *et al.* 1994), mainly due to its high intensity. A few percent of the total ionizing flux are reemitted as $H\alpha$ (Kennicutt 1989), so it is a convenient tool to trace the star formation properties of galaxies.

The main deficiency of using the $H\alpha$ line is the dust extinction. This is moderate in late-type irregular galaxies, usually some $0.2\text{--}0.4 mag$, and is much stronger in large spiral galaxies, where it may reach 3 magnitudes or more (van der Hulst *et al.* 1988). The effect should be taken into account when interpreting the $H\alpha$ data to derive the SFR in galaxies.

2 The sample

When selecting a sample of galaxies for the investigation of star formation, one should try to simplify the theoretical situation as much as possible. In our view, this can be accomplished by selecting a sample of galaxies of similar type, in which the star formation parameters should basically be the same. In order to eliminate uncertainties due to neighborhood influence on star formation, it is best to select the sample from a well-defined environment.

In addition, our aim is to isolate some of the star formation mechanisms, described above. Small objects, such as dwarf galaxies do not show spiral structure or a rotating disk. Therefore they make good candidates for our research. It is interesting, thus, to investigate a sample of dwarf galaxies in which star formation is especially vigorous.

We constructed a sample of late-type dwarf galaxies, all in the Virgo cluster area. This is a nearby region, thus the galaxies appear reasonably bright, and at a high Galactic latitude ($63^\circ \lesssim b \lesssim 80^\circ$) where the Galactic extinction is very small. In addition, as the galaxies are members of a rich cluster, the sample enables testing for the effect of cluster environment on the star formation properties of these galaxies.

Binggeli, Sandage and Tammann (1985, BST) cataloged more than 2000 dwarf galaxies in the Virgo cluster. Most objects are dwarf ellipticals, but a few hundred are late-type dwarf galaxies. Hoffman *et al.* (1987) and Hoffman *et al.* (1989) studied all late-type dwarfs in the BST sample with the Arecibo radio telescope and produced single-beam HI flux integrals and shapes of the 21 cm line. Our sample of late-type dwarfs was extracted from their list of objects with HI measurements.

In order to test the influence of hydrogen content on the star formation in the sample galaxies, we selected two subsamples dichotomized by their total HI content. In addition, to test the dependence of star formation properties on the galactic type, we separated between high surface brightness (BCD and ImIII/BCD) and low surface brightness galaxies (ImIII–ImV). We, therefore, constructed four subsamples of late-type dwarfs from the BST catalog (hereafter Virgo Cluster Catalog - VCC).

The selections criteria for the four subsamples were chosen in order to have similar numbers of objects in each group, and are characterized as follows:

1. High/high subsample: galaxies of types BCD, ImIII/BCD and HI 21cm flux integral $F_I > 1500$ mJy km/s (designated H/H, N=9).
2. High/low subsample: galaxies of types BCD, ImIII/BCD and $F_I < 500$ mJy km/s (H/L, N=7).
3. Low/high subsample: galaxies of types ImIV, ImIV/ImV, ImV and $F_I > 1000$ mJy km/s (L/H, N=4).
4. Low/low subsample: galaxies of types ImIII/ImIV, ImIV, ImIV/ImV, ImV and $F_I < 600$ mJy km/s (L/L, N=5).

The selection criteria are schematically displayed in Figure 1, and the sample galaxies, extracted from the VCC using these criteria, are presented in Table 1. The mass of the neutral hydrogen in each galaxy is directly related to its HI flux integral, and will be presented in 3.5.

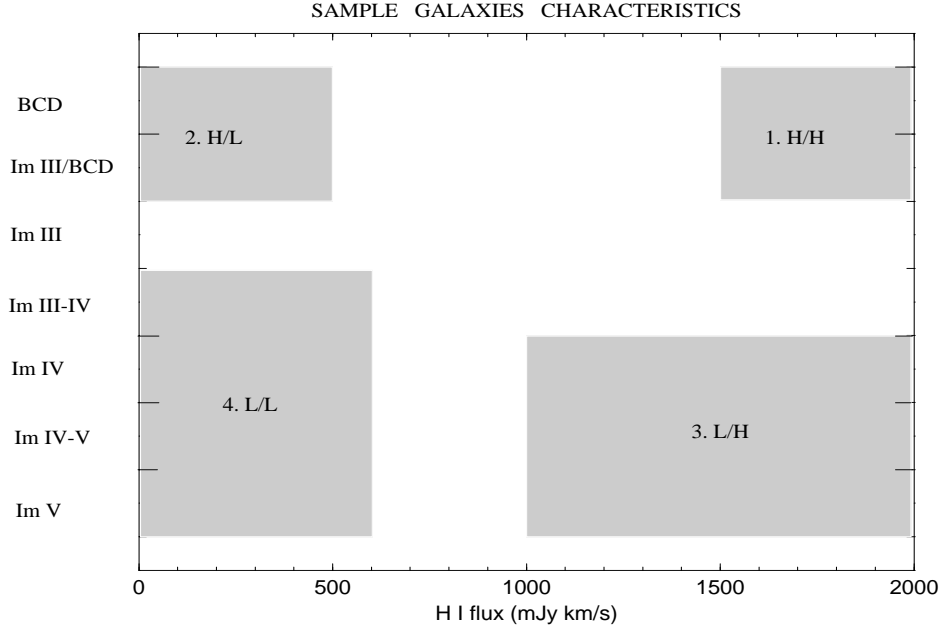


Figure 1: Distribution of the four subsamples of dwarf galaxies in the morphological type - total HI content plane. The designations H/H, H/L, L/H and L/L are explained in the text. Some "high HI" members may have $F_I > 2000 \text{ mJykm/s}$.

The intention in the dichotomy in both galactic type and HI content is to attempt to discover even weak dependence of star formation on these parameters. We expect to find a difference in the observed properties which measure recent and present star formation, such as broad-band colors and $H\alpha$ line strength, between the low and high surface brightness subsamples. We are aware of the small number of objects in each subsample, a result of the practical aspect of observations.

The spatial distribution of the sample galaxies is displayed in Figure 2. Low HI galaxies are represented by open circles, and high HI galaxies by filled circles. High HI galaxies are missing from the central region of the cluster, while low HI galaxies appear to be evenly distributed within the cluster. Although our sample is small, it supports the hypothesis of gas stripping off near the cluster core.

3 Data collection

Our data collection consists mainly of optical observations. In addition, UV observations and published information are used and presented here.

Subsample	Galaxy ID.	1950 coordinates		VCC classification	B mag	D arcmin	R (a/b)	HI flux integral mJy km/s
H/H	VCC10	12 06 51.6	13 51 06	BCD	14.5	0.81	4.46	2423
	VCC24	12 08 03	12 02 18	BCD	14.9	0.77	2.69	3538
	VCC144	12 12 44.4	6 02 24	BCD	15.3	0.44	1.90	2305
	VCC172	12 13 27.6	4 55 42	BCD:	14.5	1.07	2.23	4784
	VCC324	12 16 36.6	4 08 00	BCD	14.8	1.17	1.17	2275
	VCC459	12 18 39	17 54 54	BCD	14.9	0.63	2.34	2465
	VCC1374	12 29 05	15 08 11	ImIII/BCD	15.2	1.51	4.26	1506
	VCC1725	12 35 09	8 50 00	SmIII/BCD	14.5	1.44	1.58	1893
	VCC1791	12 36 53	8 14 12	SBmIII/BCD	14.7	1.62	1.99	6307
H/L	VCC22	12 07 51	13 26 54	BCD?	16.0	0.18	1.25	462
	VCC410	12 17 50.4	12 27 48	BCD	17.1	0.21	1.99	349
	VCC513	12 19 24.6	2 37 24	BCD?	15.1	0.53	1.20	270
	VCC562	12 20 04	12 26 05	BCD	16.6	0.44	1.25	348
	VCC985	12 24 43.2	4 32 18	BCD?	17.0	0.45	2.09	300
	VCC1179	12 26 49	10 15 54	ImIII/BCD	14.9	1.44	3.23	433
	VCC2033	12 43 33	8 44 54	BCD	14.6	0.54	1.00	410
L/H	VCC17	12 07 29	14 38 24	ImIV	15.2	1.44	1.99	2514
	VCC83	12 11 00	14 45 30	ImIII-IV	15.3	1.07	1.86	1629
	VCC1468	12 30 24.6	4 51 12	ImIV	15.0	1.26	1.73	3069
	VCC1952	12 40 34.8	7 55 24	ImIV	16.0	0.89	1.99	2375
L/L	VCC168	12 13 21.6	14 18 06	dE2/ImIV	17.0	0.53	1.20	332
	VCC260	12 15 19	5 18 12	ImIV	15.7	0.81	1.12	445
	VCC565	12 20 06	6 17 24	ImIV	15.7	0.72	1.82	473
	VCC806	12 23 00	5 05 30	ImV?	18.4	0.31		295
	VCC1013	12 24 57.6	9 36 54	ImIII-IV	16.4	0.54	1.51	265

Table 1: The sample of dwarf galaxies, from the VCC, studied here. The major axis D is in arcminutes, and the ratio between the major and minor axes is denoted by R. The HI flux integrals are from Hoffman *et al.* (1987) and Hoffman *et al.* (1989).

All optical observations were carried out at the Wise Observatory in Mizpe-Ramon, Israel. A few of the sample galaxies were observed by NB in spring 1988. During this run the galaxies were imaged using the observatory’s RCA-CCD camera. Each galaxy was measured for 10 min. through a standard V filter.

The other observations were carried out from 1991 to 1993. A general log of all the observing runs in the Wise Observatory is given in Table 2. These observations included three types of measurements: galaxy imaging in broad bands, photometry of reference stars, and galaxy imaging in H α .

3.1 Broad-band imaging

Each galaxy was imaged through B, V, R and I filters with exposure times which varied between 5 and 30 min. The RCA CCD was used in most cases, except for some runs in which the FOSC was used in imaging mode (listed in Table 2). For

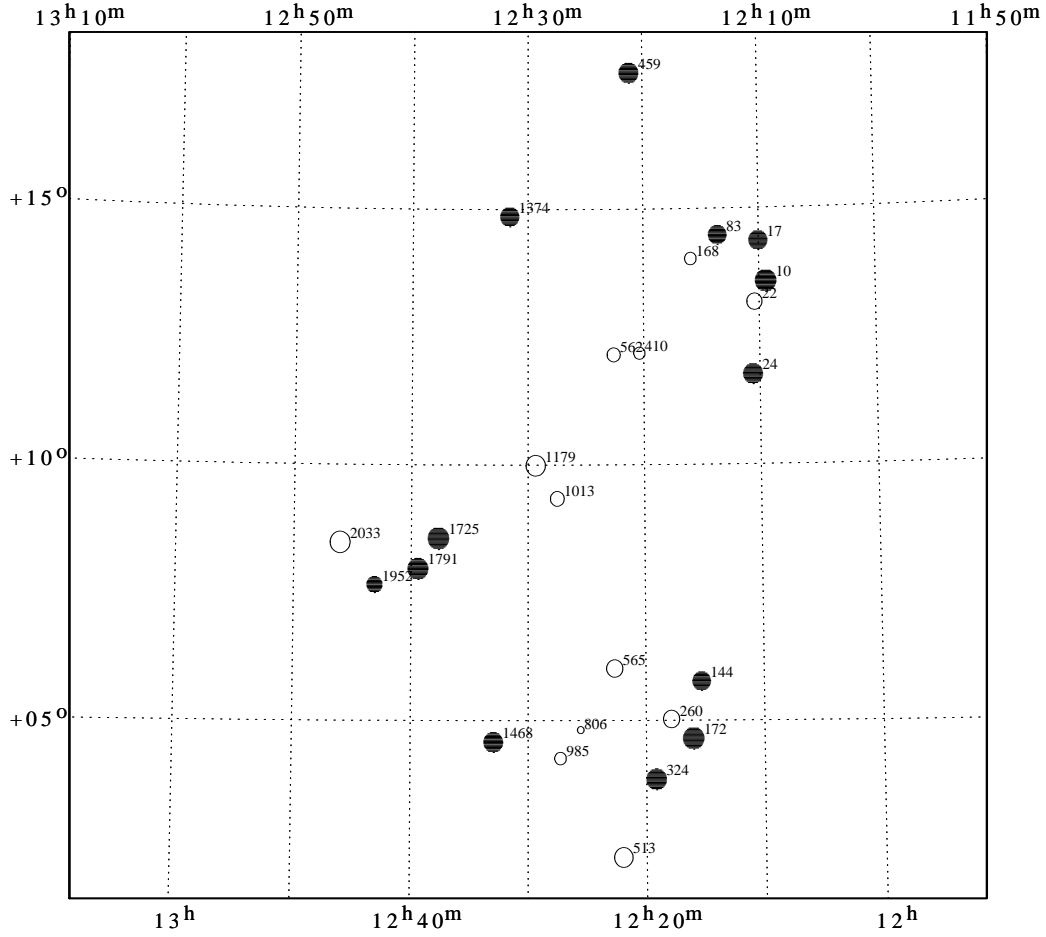


Figure 2: The sample galaxies projected on the sky. Each galaxy is labeled by its VCC number and the size of the circles indicates its B magnitude from the VCC. High HI galaxies are symbolized by filled circles and low HI galaxies by open circles.

each object a reference star close enough to appear in the galaxy’s CCD frame was selected and was imaged together with the galaxy.

3.2 Photometry of reference stars

In order to put the flux on an absolute scale, the reference stars imaged with the galaxies were measured with the Two-Channel Photometer of the Wise Observatory. We used only channel 1, with a Hamamatsu RCA C31034A photomultiplier type with a GaAs cathode in a thermoelectrically cooled enclosure.

The reference stars were chosen so that their magnitudes were in the proper range for the photometer: 10–16 *mag*. Each of the reference stars was measured through B, V, R and I filters together with photometric standard stars from the Landolt equatorial sequences (Landolt 1973, 1992).

Observation dates	Instrument used	Filters used	Remarks
19–21 Jun 90	FOSC	Broad-band imaging	
24–25 Jun 90	FOSC	Broad-band imaging	
18 Jul 90	FOSC	Broad-band imaging	
7–8 Oct 90	RCA CCD	Narrow H α imaging	
22–23 Feb 91	RCA CCD	Broad-band imaging	
24–28 Feb 91	FOSC	Narrow H α imaging	†
8–14 Mar 91	RCA CCD	Broad-band imaging	
15 Mar 91	FOSC	Narrow H α imaging	
24–25 Mar 91	RCA CCD	Broad-band imaging	
16–20 Apr 91	Photometer	Photometric calibration	
9–11 May 91	RCA CCD	Broad-band imaging	
30 Jan 92	RCA CCD	Broad-band imaging	
5 Feb 92	Photometer	Photometric calibration	
12–15 Feb 92	RCA CCD	Broad-band imaging	
25–28 Mar 92	RCA CCD	Broad-band imaging	
31 Mar–2 Apr 92	Photometer	Photometric calibration	
3–4 Apr 92	RCA CCD	Broad-band imaging	
26–27 Apr 92	RCA CCD	Narrow H α imaging	*
29 Apr–2 May 92	RCA CCD	Narrow H α imaging	
22–23 May 92	RCA CCD	Narrow H α imaging	
18–21 Feb 93	RCA CCD	Broad-band imaging	
19–20 Mar 93	RCA CCD	Broad-band imaging	
28 May 93	FOSC	Broad-band imaging	**
3 Jun 93	FOSC	Broad-band imaging	**
7–8 Jun 93	FOSC	Broad-band imaging	
11–12 Jun 93	Photometer	Photometric calibration	

* Observations by Evgeny Goldberg

** Observations by Haim Mendelson

† Observations on 24 Feb carried out under an Iraqi SCUD missile attack

Table 2: General log of Wise Observatory observations

The photometry of the reference stars requires optimal atmospheric conditions, as only then can the atmospheric extinction be accurately determined. For this reason, these measurements were repeated during several nights in order to obtain more reliable results and test their consistency.

3.3 H α measurements

Most of the sample galaxies were imaged through narrow-band filters to derive their H α emission. For each galaxy two filters were used: one which contains the H α line

("H α filter"), and the other which samples the continuum radiation adjacent to it towards longer wavelengths ("off-H α ").

One of the three H α filters listed in Table 3, which differ by their central wavelength, was used to image each galaxy according to its redshift, while the same off-H α filter was used for all galaxies. The central wavelength and width of these filters were chosen with the following requirements:

1. There is no overlap between the off-H α and any of the H α filters, while this bandpass is still close enough to the line for sampling directly the continuum radiation,
2. There are no significant spectral lines in the bandpass of the off-H α filter,
3. The H α filters cover the range of velocities of the Virgo cluster ($\sim 0 - 2500$ km/s), while any H α line emitted within this velocity range falls in one of the filters' bandpass within at least 90% of its peak transmission.

Filter ID.	λ_0	$\Delta\lambda$ (FWHM)	Peak transmission
H α - 2	6562Å	50Å	67.5%
H α - 3	6586Å	48Å	66.0%
H α - 4	6610Å	55Å	69.7%
off-H α	6700Å	53Å	70.0%

Table 3: The main characteristics of the H α filters used at the Wise Observatory.

As these are interference filters, their transmitted bandpass depends on the incidence angle of the incoming radiation, and the characteristics described above are for zero incidence angle. The observations were carried out, however, with the CCD placed in the focal plane of the f/7 converging beam of the telescope. This means that the rays are incident on the filters with angles varying between $1.8 - 4^\circ$. In order to check this effect, the filters' response curves were measured at the laboratories of the Applied-Physics Department at Tel-Aviv University using several incidence angles. The results of this measurement showed that the central wavelength of the three H α filters was shifted by 1.5Å to the blue relative to the nominal normal incidence central wavelength, while the off-H α was shifted by 3.8Å blueward. These changes are not significant for our measurements, as the H α line of each galaxy departs from the central wavelength of the appropriate filter by no more than 12Å . This puts the H α line in an effective transmission of $\sim 88\%$ or more of the peak of the filter, while for most galaxies it is at least $\sim 95\%$.

For each of the galaxies, at least two 20 min exposures were obtained through each of the two filters. In addition, a spectrophotometric standard star (HZ44) was measured several times each night through different air masses with the same filters, in order to derive the atmospheric extinction and absolute photometric calibration for the H α images.

3.4 UV observations and data

Seven of the sample galaxies were observed with the IUE, two of them in 1986 within the US program EGITT. The other five were observed by EA in 1991 and 1993. The observations took place at the VILSPA tracking station, Spain, and each galaxy was observed for a full VILSPA observing shift, ~ 6 hours of integration. In all cases the spectrum was obtained through the IUE large aperture, which is a $\sim 10'' \times 20''$ oval, using the short wavelength camera (SWP) - low dispersion setup, which covers the spectral range of 1200–1950Å.

In late March 1992 the ATLAS-I space shuttle mission took place, during which UV observations were carried out with the shuttle-borne telescope FAUST (*Fusée Astronomique pour l'Ultraviolet STellaire* or *FAr Ultraviolet Space Telescope*). This UV imaging instrument was developed jointly by the Laboratoire d'Astrophysique Spatiale of the CNES, and the Space Astrophysics Group at Berkeley. The FAUST UV bandpass has $\bar{\lambda} \simeq 1650\text{Å}$ with $\Delta\lambda \simeq 400\text{ Å}$. During the ATLAS-I mission it imaged a number of $\sim 8^\circ$ wide sky areas, among which are three overlapping frames of the Virgo cluster. These FAUST frames were used to obtain UV data for the dwarf galaxies in our sample.

Telescope	Object	J2000 coordinates		Date
IUE	VCC2033	12 46 04.7	08 28 31.1	9 Jul 86
	VCC324	12 19 09.9	03 51 21.0	10 Jul 86
	VCC10	12 09 24.7	13 34 24.6	18 May 91
	VCC24	12 10 36.1	11 45 36.8	19 May 91
	VCC22	12 10 24.1	13 10 12.8	22 May 91
	VCC144	12 15 17.7	05 45 43.9	19 Jan 93
	VCC562	12 22 36.3	12 09 27.3	20 Jan 93
FAUST	Virgo-north	12 ^h .506	15° .50	24 Mar 92
	Virgo-center(M87)	12 ^h .508	12° .82	27 Mar 92
	Virgo-south	12 ^h .463	10° .15	28 Mar 92

Table 4: UV observations of the sample galaxies and the Virgo cluster.

The UV observations of Virgo dwarf galaxies are listed in Table 4.

3.5 Additional data

A few of the sample galaxies were detected by IRAS and appear in the IRAS point source catalog. The IRAS data consist of flux densities in four infra-red (IR) bands centered at 12 μm , 25 μm , 60 μm and 100 μm . IRAS has scanned the entire celestial sphere, and some areas were scanned several times. It is possible to co-add the various IRAS scans at a given location to obtain a deeper detection or upper flux limit at this location in the sky, for the four IRAS bands. Such co-adding was done by NB

for the objects of our sample which do not appear in the IRAS catalog, at the IRAS archives of the Rutherford-Appleton Laboratory, England.

For every galaxy of the sample, except for VCC806 and VCC1013 where observations were not possible due to software problems, we have IRAS data, either as absolute fluxes or as upper limits of flux. In addition, some objects are FIR sources in the IRAS Faint Source Catalog. Their flux densities together with the other galaxies data are listed in Table 5, but without errors. The typical error of the FSC, for faint IRAS sources, is $\sim 15\%$ of the listed flux density.

As mentioned above, our sample is based on the studies of Hoffman *et al.* (1987) and Hoffman *et al.* (1989) with the Arecibo radio telescope. In these publications, each sample galaxy has its HI flux integral 21cm quoted along with the heliocentric velocity v_{\odot} and velocity dispersion derived from the HI line width at 20% of peak height - $\Delta V(20\%)$. We calculated the HI mass following the prescription in the Third Reference Catalog of Bright Galaxies (de Vaucouleurs *et al.* 1991), as:

$$M_{HI} = 235.5 S_{HI} D^2 \quad (1)$$

where M_{HI} is in M_{\odot} , S_{HI} is the HI line flux integral in mJy km/s and D is the distance to the object in Mpc.

In order to derive the HI mass of these galaxies, a common distance is adopted for all objects. A value of 18 Mpc may well represent the average distance of galaxies in the Virgo cluster (e.g., Fouqué *et al.* 1990), and is the value adopted here. No more accurate information is available on the distance to the type of galaxies discussed here (such as a Tully-Fisher relation), and in any case, such a relation is usually very dispersed for irregular galaxies and the uncertainties are large. We adopt, therefore, a distance of 18 Mpc and bear in mind that the uncertainty in this distance is up to $\sim 15\%$. These values, together with the IRAS data, are given in Table 5.

4 Data reduction

All data reduction was performed at the Wise Observatory headquarters at Tel-Aviv University. The CCD images were reduced with the VISTA image-processing software package, described by Pogge *et al.* 1988. Photometric data was reduced with the observatory's photometry package.

As an initial step all the CCD frames, narrow and broad-band, were 'zapped' to remove cosmic ray hits and bad pixels. Then, for each run, an averaged BIAS frame was constructed, together with normalized sky flat-field frames for every bandpass. The images of the galaxies were de-biased and flat-fielded using these reference frames.

4.1 Broad-band colors

Galaxy ID.	HI flux integral mJy km/s	$\Delta V(20\%)$ km/s	v_{\odot} km/s	HI mass ^a M_{\odot}	IRAS flux densities (Jy)			
					12 μm	25 μm	60 μm	100 μm
VCC10	2423	209	1965	1.85×10^8	< 0.11	< 0.18	0.19 ± 0.04	0.43 ± 0.17
VCC24	3538	236	1280	2.7×10^8	< 0.08	0.09[1.4]	0.09[1.7]	< 0.30
VCC144	2305	135	2011	1.76×10^8	0.150	0.31	0.62 ± 0.04	0.660 ± 0.09
VCC172	4784	164	2194	3.65×10^8	0.136	0.192	0.228	0.501
VCC324	2275	72	1508	1.74×10^8	0.115	0.171	0.72 ± 0.06	0.823
VCC459	2465	150	2103	1.88×10^8	0.072	0.128	0.236	0.543
VCC1374	1506	124	2560	1.15×10^8	< 0.12	0.15[1.6]	0.13[2.4]	0.55[4.2]
VCC1725	1893	114	1051	1.44×10^8	0.06[1.2]	0.10[1.1]	< 0.18	0.35[2.4]
VCC1791	6307	138	2057	4.81×10^8	0.120	0.228	0.271	0.631
VCC22	462	86	1691	3.53×10^7	< 0.18	< 0.13	< 0.14	< 0.26
VCC410	349	68	274	2.66×10^7	< 0.11	< 0.19	< 0.11	< 0.32
VCC513	270	130	1828	2.06×10^7	0.222	0.226	0.610	1.161
VCC562	348	–	45	2.66×10^7	< 0.12	< 0.18	0.14[1.6]	< 0.26
VCC985	300	67	1645	2.29×10^7	< 0.12	< 0.20	< 0.15	< 0.26
VCC1179	433	142	777	3.3×10^7	0.112	0.174	0.298	0.758
VCC2033	410	50	1508	3.13×10^7	< 0.11	0.10[1.3]	0.20 ± 0.05	< 0.35
VCC17	2514	69	823	1.92×10^8	< 0.09	< 0.15	0.13[2.5]	0.46[2.7]
VCC83	1629	119	2443	1.24×10^8	0.07[1.2]	0.13[2.0]	0.10[2.3]	< 0.57
VCC1468	3069	107	1234	2.34×10^8	0.06[1.5]	< 0.24	< 0.18	< 0.39
VCC1952	2375	74	1325	1.81×10^8	< 0.15	< 0.24	< 0.15	0.25[2.3]
VCC168	332	72	685	2.53×10^7	< 0.18	< 0.18	< 0.18	< 0.78
VCC260	445	84	1783	3.4×10^7	< 0.21	< 0.15	< 0.39	
VCC565	473	68	868	3.61×10^7	< 0.18	0.17[1.9]	< 0.15	< 0.57
VCC806	295	99	2433	2.25×10^7				
VCC1013	265	71	1691	2.02×10^7				

^a calculated using a common distance of 18 Mpc

Table 5: IRAS and radio data of the VCC sample galaxies

4.1.1 Reference star photometry

The photometer data were reduced with a composite extinction-transformation program. This program computes instrumental magnitudes and colors and fits them by least-squares to the catalog values of the standard stars. The fit is linear in air mass and second-order in colors. The instrumental magnitudes and colors are taken as:

$$\begin{aligned}
v &= a_0 + a_1 Am + V + a_2(B - V) + a_3(B - V)Am + a_4(B - V)^2 \\
(b - v) &= b_0 + b_1 Am + b_2(B - V) + b_3(B - V)Am + b_4(B - V)^2 \\
(v - r) &= c_0 + c_1 Am + c_2(V - R) + c_3(V - R)Am + c_4(V - R)^2 \\
(r - i) &= d_0 + d_1 Am + d_2(R - I) + d_3(R - I)Am + d_4(R - I)^2
\end{aligned} \tag{2}$$

where Am is the air mass, v , $(b - v)$, $(v - r)$ and $(r - i)$ are instrumental values, and V , $(B - V)$, $(V - R)$ and $(R - I)$ are catalog magnitudes and colors. a_0, b_0, c_0 and d_0

are constants which depend on the instrument. a_1, b_1, c_1 and d_1 are the atmospheric extinction coefficients in the appropriate bands, while a_3, b_3, c_3 and d_3 account for the dependence of the extinction on the stellar color, which originates from the variation of atmospheric extinction across the filters' transmission band. The other coefficients account for possible difference between the standard Johnson-Kron-Cousins B,V,R and I bands (e.g., Landolt 1992) and the instrument effective response (filters + cathode quantum efficiency).

As mentioned before, the photometric observations were repeated during several nights for most of the reference stars. Each night was ranked according to the goodness of fit of the standard stars parameters. The results of the different nights were consistent, in almost all cases, within the measurement error, and for each reference star the result from the 'best' night was adopted.

4.1.2 Galactic color indices

The broad-band images of every sample object were merged to produce a final frame with the best S/N available in each band. In some cases, a frame or two were excluded from the reduction due to very low S/N. Their inclusion would not have increased the total S/N ratio but rather lowered it, because of the considerable additional noise introduced in the summed images, in comparison with the low additional signal.

The object's total intensity was measured on each final frame, together with the total intensity of the corresponding reference star. Since the objects are irregularly shaped galaxies, no model fitting to their shape could usually be done. Therefore, an empirical way was adopted, as follows:

A polygonal area, which contains the entire object as determined by visually inspecting the image, is constructed manually upon the displayed image, using the deepest of the four available images of that object. The guideline for setting the polygon border is that the signal-to-noise ratio for each pixel of the object's image falls well below unity, while trying not to include too much of the sky noise. This corresponds to a typical surface brightness of $\sim 27 \text{ mag}/\square''$ in V, depending on the total exposure time of the image and the sky level.

The total counts within this region are summed-up and the appropriate sky background (the sky value times the number of pixels within the polygon) is subtracted, to yield the net object counts. An example of a galaxy image with the polygon which surrounds it is shown in Figure 3.

The sky value and σ_{sky} (standard deviation of a single pixel's value from the sky level) were calculated using the SKYALL procedure within VISTA (Almoznino *et al.* 1993). This procedure adopts the most probable intensity value of the frame as the sky value.

To calculate the error in the net object counts we use standard Poissonian statistics for the number of photons collected by the detector, namely $\delta n = \sqrt{n}$, where δn is the error of the n photons. This corresponds to I counts, where $G = \frac{n}{I}$ is the gain

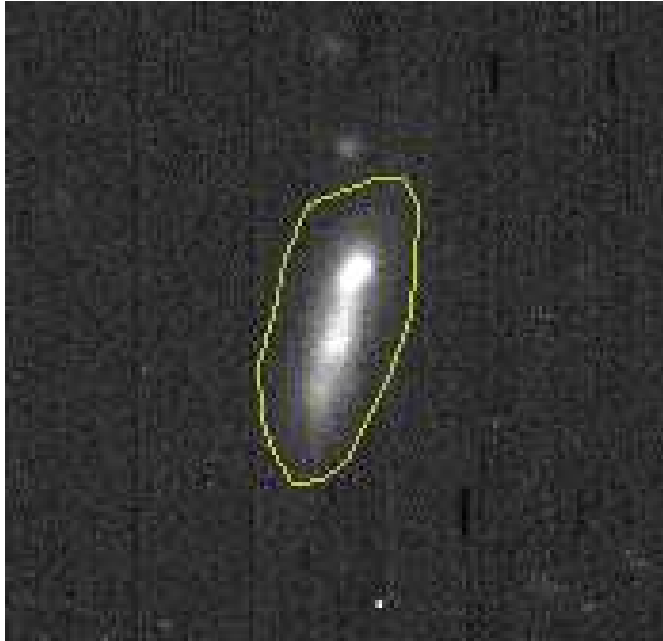


Figure 3: The image of VCC1374, with the surrounding polygon used for measurement.

of the instrument, ($15 \frac{\text{photons}}{\text{count}}$).

In addition, σ_{sky} contributes to the error in the measured value of I , thus:

$$\Delta I = \sqrt{\frac{I}{G} + 2P\sigma_{sky}^2} \quad (3)$$

where P is the number of pixels within the polygon used for measurement. Note that the readout noise of the instrument is not included in the equation. This is because the σ_{sky} , which is measured empirically, consists of both the photon statistics error of the sky level and the readout noise, and there is no need to a-priori estimate the latter.

The reference star was measured in the same way as the object, only within a $D = \sim 20$ arcsec circular 'aperture' centered on the star, instead of a polygon. The sky value was measured within a $\sim 90 \times 90$ pixel box around the star.

Having the magnitudes of the reference star in each band measured photometrically, it is possible to obtain the corresponding magnitudes of the object directly from the CCD frames from the ratio of intensities. Actually, the derived quantities were the V magnitude and the color indices B-V, V-R and R-I. The advantage of this method is that observations of the sample galaxies, which consume large amounts of telescope time, do not require any special observing conditions, since both the object and the reference star appear on the same CCD frame, and the measurement is relative. The assumption here is that scattered clouds, which sometimes affected the

observations, can be considered ‘gray’ attenuators which do not modify the measured color properties. This is justified, considering the size of typical water droplets or ice particles in these clouds, which is significantly larger than the wavelength of observation. Another effect, that may be influencing the results, is the possible difference between the effective response of the CCD+filters observing system and the standard Johnson-Kron-Cousins system. The implications of this effect on the derived color indices of the galaxies are discussed below.

The object V magnitude is given by:

$$m_v = -2.5 \log \left(\frac{I_o}{I_s} \right) + V_{phtm} \quad (4)$$

where I_o is the object CCD intensity, I_s is the reference star CCD intensity, and V_{phtm} is the reference star V *mag* from the photometric measurement. The error of the derived magnitude is the root-mean-square combination of the individual errors:

$$\Delta m_v = \sqrt{1.0857^2(\delta_o^2 + \delta_s^2) + \Delta_{phtm}^2} \quad (5)$$

where $1.0857 = 2.5 \log_{10} e$, $\delta_o = \frac{\Delta I_o}{I_o}$ and $\delta_s = \frac{\Delta I_s}{I_s}$ are the relative errors of the object and star CCD intensity, and Δ_{phtm} is the error of the photometric result.

The object color indices and their errors are derived in the same way as the V magnitude, except that intensity ratios between two CCD frames are used, instead of intensities. In a single case (VCC 1468) the I band image had a very intense and nonuniform sky background relative to the low object signal, causing an unreliable R–I result of -0.25 . This result is displayed in Table 6, but is not included in graphic presentations of the results.

In cases when the reference star appeared saturated on the CCD image of the galaxies, and other stars in the field were too faint to be measured by the Wise photometer, use was made of intermediate frames. In these frames, which were obtained with a short exposure time, the primary reference star is not overexposed but the galaxy is underexposed. A second, fainter, star (not overexposed on the long-exposure object frames) was measured on these frames using exactly the same method as for the object. The results are then used (and referred to as “*phtm*” data) with the object CCD images to yield the object’s magnitudes and colors.

In addition to broad-band magnitudes and colors, approximate monochromatic magnitudes at $0.44 \mu m$, $0.55 \mu m$, $0.64 \mu m$ and $0.79 \mu m$ were obtained from the broad-band data. This was done using the corresponding data for flux densities at the central wavelength of B, V, R and I broad-bands for a normal zero-magnitude star from Bessel (1979). The flux density for a galaxy at a wavelength that corresponds to a certain band i is given by $F_{g,i} = F_{s,i} \times 10^{-0.4 m_{g,i}}$, where $F_{s,i}$ is the flux density of the zero-magnitude star and $m_{g,i}$ is the broad-band magnitude of the galaxy at band i . The flux densities are converted to monochromatic magnitudes by: $m_\lambda = -2.5 \log[F_\lambda(\text{erg/s/cm}^2/\text{\AA})] - 21.175$. The errors are the same as the

corresponding broad-band errors. These monochromatic magnitudes are useful for combination with other spectral ranges, to produce a broad coverage of the spectral energy distribution (SED) of the sample galaxies.

4.2 H α flux measurements

The purpose of observing the galaxies in H α is to measure the line emission from each galaxy. However, any filter, even centered on a spectral line, admits a significant contribution from the continuum. This is the reason for observing each galaxy through two filters: one centered on the line (H α filter) and another rejecting emission lines and (presumably) sampling the continuum (off-H α). The H α line flux is the difference between the flux contributions sampled by these two filters. The procedure entails the determination of the flux *density* of the continuum (sampled by the off-H α filter), scaled to the transmission profile of the H α filter, and its subtraction from the flux measured by the latter filter.

In order to derive the absolute fluxes of the objects, the atmospheric extinction should be compensated. This is done using the results for the spectrophotometric standard star, which was measured through different air masses during the same night of observation. Naturally, this type of reduction uses magnitudes rather than fluxes. Only after the atmospheric extinction is taken care of, can fluxes be derived.

The H α data consist of at least two frames in the H α filter and two in the off-H α filter, for each of the sample galaxies. In contrast to the broad-band data where frames were combined, each frame was reduced to yield a separate monochromatic magnitude for the object.

The frames were shifted to match the broad-band images, and each of the galaxies was measured inside the same polygonal area used for its broad-band image. The method of measurement was basically the same as for the broad-band frames, with the exception that the sky background level was computed several times using different sky 'boxes' around the objects. This was because the signal from the galaxies was very weak in a 50Å narrow band, and slightly different sky values may make a difference in the results. The mean of these results was adopted as the object counts, while the error was usually taken as the largest of the errors of each measurement. The standard deviation of the results was normally smaller than this, but whenever it was larger - it was adopted as the error. In some cases the result was consistent with zero, mostly in the off-H α band.

As mentioned above, the spectrophotometric standard HZ44 was used for the calibration of the H α data. This star is a hot white dwarf, devoid of strong Balmer lines, and thus, suitable for our purposes. HZ44 was measured through a 'circular aperture' on each of its frames to yield total counts in the corresponding narrow-band and for each airmass.

Both the object counts and the standard star counts were then converted to instrumental magnitudes by:

$$m_{inst} = -2.5\log(C) , \quad \Delta m = 1.0857\frac{\Delta C}{C} \quad (6)$$

where C and ΔC are the counts result and its error.

The next stage was to obtain monochromatic magnitudes of the objects in the two narrow bands. The reduction relies on the monochromatic magnitudes of HZ44, taken from Massey *et al.* (1988), where the stellar spectrum is convolved with 50Å wide bands, separated by 50Å. In order to obtain the monochromatic magnitudes in the central wavelengths of our narrow-band filters a spline interpolation was performed on the available spectrophotometric data. The following results were obtained for HZ44: $m_{6562} = 12.20$, $m_{6586} = 12.16$, $m_{6610} = 12.12$, $m_{6700} = 12.16$.

The atmospheric extinction was calculated separately for each band and for every night of observation, from the several available images of HZ44. Here the relation between the instrumental magnitude in a certain narrow-band i and the real monochromatic magnitude m_i is simply:

$$m_{inst,i} = m_i + a_{0,i} + a_{1,i}Am \quad (7)$$

Using the constants $a_{0,i}$ and $a_{1,i}$ (which may be different every night) the monochromatic magnitudes of the galaxies were computed for the H α and the off-H α bands. In this, we assume no change in the atmospheric extinction across the 50Å transmitting band and that the effective central wavelength of the filters does not depend on the object spectrum.

Next, for each object, a mean flux result was calculated for each of the two bands, using the available flux results for this band. The mean was weighted according to the errors of each result (weight= $1/\sigma^2$ where σ is the error) and the error is the largest of the error of the mean and the standard deviation from the mean. The *total* flux obtained through the H α filter is its flux density times the effective filter width. The shape of the transmission curves of our narrow-band filters indicates that their FWHM represents well their effective width, thus, the FWHM of the filters listed in 3.3 was adopted as their effective width.

To obtain the net H α line flux, the continuum contribution is subtracted from the total H α band flux. This radiation is sampled by the off-H α filter. However, this may not represent the exact amount of continuum radiation at the H α band, as the continuum flux itself gradually changes with wavelength. This effect is small, but may be significant in the case of H α faint galaxies. To compensate for this, the rough SED from the broad-band data was considered (its derivation is described in 5.3). The monochromatic magnitudes at 0.55 μm and 0.79 μm , derived from the V and I magnitudes, were linearly interpolated to yield a rough, gradual change across the spectral region between them. This information was used to obtain the expected change in continuum radiation between the two H α narrow bands. The R band magnitude was not used since it contains the H α line and may be misleading.

The SEDs of the galaxies are displayed in Figures 5, 6, and 7. For all the sample galaxies the SED decreases with increasing wavelength, and the relative change of the continuum radiation between the off-H α and H α bands is from 0 to 2.5%. For the H α -bright galaxies, the H α flux may be as high as twice that of the off-H α band and clearly the effect of continuum sloping is insignificant, as the accuracy of our measurements is of order of 5%. For H α -faint galaxies, however, taking this effect into account can change our interpretation for a certain object, from a significant H α flux to \sim zero H α flux.

If we denote the expected ratio between the H α band *continuum* flux and the off-H α flux, as derived by the above procedure, by R , the net H α line flux is given by:

$$F(H\alpha) = (F_{H\alpha} - R \times F_{off})FW_{H\alpha} \quad (8)$$

where $F_{H\alpha}$ and F_{off} are the flux densities obtained through the two bandpasses, and $FW_{H\alpha}$ is the FWHM of the H α filter.

The H α equivalent width is given by:

$$EW[H\alpha] = \frac{F(H\alpha)}{R \times F_{off}}FW_{H\alpha} \quad (9)$$

It should be noted that all the H α fluxes and equivalent widths derived here are actually H α + [N II] fluxes and equivalent widths, as the filters used include also the accompanying nitrogen $\lambda\lambda$ 6548, 6583Å lines. This will be discussed later in more detail.

Using the total flux, the H α flux per unit solid angle was derived for each galaxy. The angular size of the galaxies was determined by constructing a confining polygon around the galaxy, with its border set to a S/N \sim 1. The border was set on the deepest image of each object and it corresponds to $\sim 25 \text{ mag}/\square$ in B.

4.3 UV data reduction and combination with optical data

As mentioned in section 3.4, two types of UV data were collected for the sample galaxies: IUE spectral data and FAUST imaging data. Our aim is to construct a SED for as many galaxies as possible from the sample. For this, a derivation of UV monochromatic magnitudes was performed at Wise Observatory.

4.3.1 IUE data

For the five galaxies observed during 1991 and 1993 the spectra were re-derived from the photometrically corrected IUE images. Reseau marks and 'hot pixels' were interpolated over, to obtain more reliable spectra of the objects. The spectra of all the galaxies were faint and noisy, and no spectral lines were clearly visible. To obtain the continuum flux, the spectra were convolved with a 30Å wide Gaussian, and only

the smoothed spectra were considered. This was performed also for the two sample galaxies observed in 1986, where the Uniform Low-Dispersion archive spectra were used.

The smoothed spectra were measured in two 100\AA wide 'bandpasses', centered at 1350\AA and 1850\AA . The error of these measurements was estimated to be between 15% and 20% according to the noise at each band. For two objects (VCC562 and VCC2033) this procedure yields \sim zero flux, and their spectra were not reduced further. A conversion was made from F_λ to monochromatic magnitudes according to $m_\lambda = -2.5 \log[F_\lambda(\text{erg/s/cm}^2/\text{\AA})] - 21.175$. The error was calculated as in eq. 6.

The IUE large aperture is $\sim 10'' \times 20''$ in size. Therefore, the spectrum we obtained does not represent the radiation emitted by the entire galaxies, but rather the energy from their bright regions. However, because the galaxies in our sample are small in size, most or all of the radiation comes from a region of that size.

In order to ensure that no bias is present in the results, the optical broad-band images of the galaxies with IUE data were sampled through 'ovals' as similar as possible to the IUE aperture, in size, shape and orientation during the IUE exposure (the orientation of the IUE elongated entrance aperture changes with time, because of the solar angle constraint for the proper illumination of the spacecraft solar panels). The reduction was the same as in 4.1.2, with the exception that the area of sampling was different. Monochromatic magnitudes in the optical were derived for the central regions of these galaxies to produce a meaningful combination with the UV data and a reliable SED of the galaxies.

The above treatment was not performed for VCC324=MRK49, which is too large ($\sim 40''$). Because of its size, a small change in the location, orientation or size of the artificial oval used for sampling, may lead to great changes of the final result, which, in turn, may lead to an error in the derivation of the SED. Therefore, the UV data for this galaxy was discarded.

4.3.2 FAUST data

As mentioned above, three fields in the Virgo cluster were imaged by the FAUST instrument. Each field is about 8° in diameter and together they cover most of the cluster. A merged picture of the three images is shown in Figure 4. The full analysis of the FAUST observations of the Virgo region is the subject of a different paper (Brosch *et al.* 1996). Note also that a general catalog of FAUST sources was produced by automatic correlations against existing catalogs (Bowyer *et al.* 1995).

The FAUST images underwent flat-fielding corrections at Berkeley, to obtain frames in calibrated units of FAUST-counts per second. Each frame was compared to a predicted UV map of the corresponding area of the sky, derived from the SAO catalog (Shemi *et al.* 1993), in order to identify the SAO stars in it. These were used to derive the transformation from the image pixel coordinates to celestial coordinates. About 15 stars were used in each frame, and the standard deviation of the calculated

VIRGO - FAUST merged image

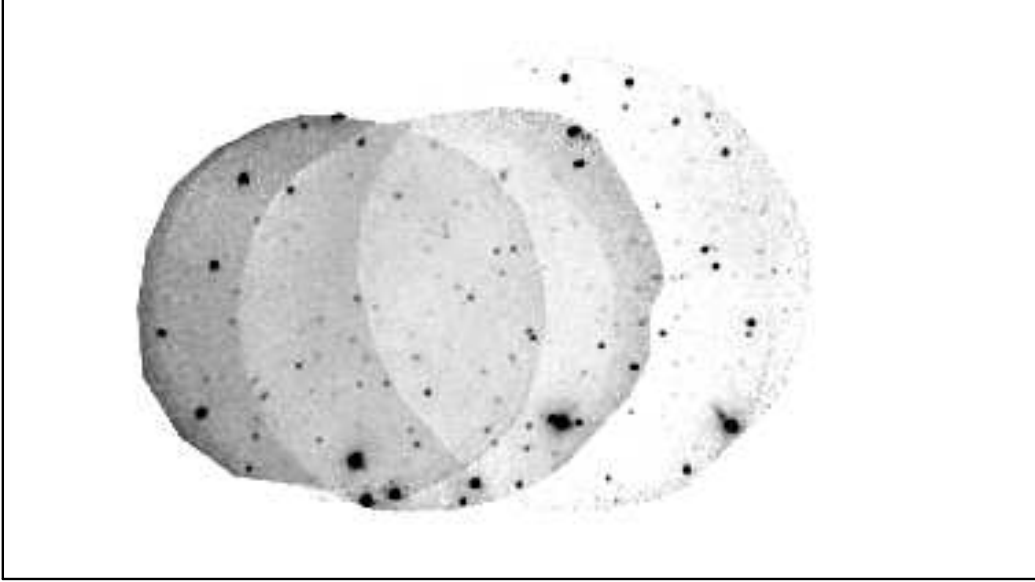


Figure 4: Merged picture of the three FAUST Virgo fields. Each field is $\sim 8^\circ$ wide, west is up and north is to the left.

coordinates from the real ones was $\simeq 0'.5$ (0.45 pixel).

The expected location of every sample object was found on the frames using these transformations. At each location 'aperture photometry' was performed in much the same method as for the reference star measurement in 4.1, with the exception that the error calculation did not take the photon-statistics error into account. This is because in this type of frames the sky noise dominates the error of the measurement in comparison with other effects.

Two of the sample galaxies were reliably detected on the FAUST frames: VCC1725 and VCC1791. The aperture photometry was performed at all the expected locations of the sample objects, regardless of whether an object was visible there or not. Thus, for most objects, an upper limit for the UV radiation was derived. Whenever an object was expected to appear in more than one FAUST frame, its location was measured separately on each frame. Results for objects close to the image edges were ignored, due to very low S/N, and a 1σ upper limit was derived whenever the accuracy was worse than 30%. For objects which had more than one acceptable result, the 'best' result was adopted, i.e., the lowest upper limit value.

Unfortunately, the two objects which were detected appeared only on one frame, so no cross check for galaxy fluxes was possible. However, cross checks between the three frames were carried out using other objects which appear in two, or even all three images, yielding good agreement between their different count results: disregarding very bright objects, in which case distortions arise, 90% of the objects have values

that differ by less than 1.5σ from each other.

The results were then transformed to approximate monochromatic magnitudes at 1650\AA using the calibration from Brosch *et al.* (1995):

$$m_{FAUST} = m_{inst} + 11.62 \quad (10)$$

where m_{inst} and its error are the same as in equation 6.

It should be noted that only two galaxies were both measured by IUE *and* are within the field of view of FAUST. These are VCC562 and VCC2033, which have FAUST UV upper limits consistent with the $S/N \ll 1$ in their IUE spectra. Therefore, a cross check between FAUST and IUE results is not available with our galaxies.

5 Results

5.1 Broad-band magnitudes and colors

In general, the V magnitude of the galaxies lies within a range of $\sim 0.6 \text{ mag}$ of their listed blue magnitude from the VCC. Caution should be exercised when comparing our results with other published data, since most of the photometric observations of these galaxies were carried out through apertures with various diameters, between $19''$ and $120''$ (Hunter and Gallagher 1985, Gallagher and Hunter 1986, Gallagher and Hunter 1989, Drinkwater and Hardy 1991). Our results are mostly within 2σ of other results, except for the larger galaxies, VCC324=Mrk49, VCC1791, VCC2033 and VCC1179, for which we obtained magnitudes brighter by $\sim 0.4\text{--}1.2 \text{ mag}$ than other published data. The first three can be explained by the aperture size used in previous studies, which does not include the entire galactic flux. For VCC1179, however, Gallagher and Hunter (1986) have obtained $V=16.13 \text{ mag}$ through a $30''$ aperture, whereas our result is 15.59 ± 0.04 . Considering their aperture size, a difference of $\sim 0.25 \text{ mag}$ is expected, so the discrepancy is still 0.3 mag for this object.

The broad-band colors of the galaxies were obtained through comparative photometry on CCD images, together with absolute photometry of the reference stars. The reference stars' data are calibrated according to the standard Johnson-Kron-Cousins bands, but the CCD photometry did not take into account the possible difference between the CCD filters and the standard. However, if the CCD+filters observing system has a nonzero color term, it affects the results only through the color *difference* between the measured galaxy and the reference star on the CCD frames. In other words, if the galaxy is measured to have the same CCD colors as the reference star, then its true colors are the same as the star's, provided that the color term is not drastically large. The color differences between the sample galaxies and the stars were mostly in the range of $0.0 - 0.2 \text{ mag}$ in all colors. This means that a color term as large as 0.15 will cause an error of up to 0.03 mag in the results, which is the typical error in our data. From a number of observations carried out in 1993, the

Wise-Observatory RCA CCD was found to have color terms of up to 0.15 (in B–V, Heller 1993, private communication). The change in colors due to this effect is, thus, not markedly significant in our case and we conclude that the broad-band results are reliably representing the observed standard color indices of these galaxies.

Group	VCC no.	V mag.	B–V	V–R	R–I
H/H	10	15.56 ± 0.08	0.64 ± 0.10	0.68 ± 0.10	0.42 ± 0.08
	24	15.37 ± 0.03	0.75 ± 0.03	0.48 ± 0.07	0.49 ± 0.05
	144	14.83 ± 0.03	0.46 ± 0.03	0.22 ± 0.02	0.23 ± 0.02
	172	14.86 ± 0.03	0.52 ± 0.02	0.33 ± 0.02	0.26 ± 0.02
	324	14.02 ± 0.03	0.56 ± 0.02	0.40 ± 0.01	0.25 ± 0.01
	459	14.67 ± 0.05	0.62 ± 0.02	0.27 ± 0.09	0.39 ± 0.02
	1374	14.53 ± 0.03	0.47 ± 0.02	0.34 ± 0.01	0.37 ± 0.02
	1725	14.78 ± 0.03	0.40 ± 0.05	0.30 ± 0.03	0.42 ± 0.03
	1791	14.38 ± 0.03	0.47 ± 0.05	0.29 ± 0.02	0.33 ± 0.02
H/L	22	16.22 ± 0.03	0.61 ± 0.03	0.40 ± 0.07	0.46 ± 0.05
	410	17.20 ± 0.04	0.56 ± 0.04	0.37 ± 0.04	0.40 ± 0.04
	513	15.19 ± 0.03	0.65 ± 0.02	0.63 ± 0.01	0.60 ± 0.01
	562	16.19 ± 0.03	0.40 ± 0.03	0.33 ± 0.07	0.53 ± 0.05
	985	16.00 ± 0.05	0.62 ± 0.03	0.39 ± 0.09	0.50 ± 0.03
	1179	15.59 ± 0.04	0.39 ± 0.06	0.53 ± 0.04	0.43 ± 0.03
	2033	14.96 ± 0.03	0.65 ± 0.05	0.42 ± 0.03	0.40 ± 0.04
	L/H	17	15.85 ± 0.03	0.58 ± 0.04	0.23 ± 0.07
	83	15.67 ± 0.03	0.61 ± 0.03	0.53 ± 0.07	0.54 ± 0.05
	1952	16.51 ± 0.03	0.63 ± 0.03	0.40 ± 0.02	0.31 ± 0.03
	1468	15.89 ± 0.03	0.54 ± 0.05	0.24 ± 0.03	-0.25 ± 0.21
L/L	168	17.58 ± 0.08	0.76 ± 0.17	0.62 ± 0.10	0.29 ± 0.09
	260	16.77 ± 0.04	0.47 ± 0.05	0.41 ± 0.08	0.41 ± 0.06
	565	16.89 ± 0.05	0.53 ± 0.06	0.45 ± 0.05	0.43 ± 0.04
	806	18.80 ± 0.12	0.57 ± 0.17	0.32 ± 0.16	0.38 ± 0.26
	1013	16.85 ± 0.06	0.52 ± 0.05	0.40 ± 0.10	0.45 ± 0.03

Table 6: Broad-band magnitudes and color indices of the sample.

The broad-band data of the galaxies are given in Table 6. These broad-band colors are the *observed* values, and are not corrected for internal dust extinction (the Galactic extinction is very small in the direction of Virgo). The issue of internal dust extinction will be discussed in a subsequent paper.

5.2 H α fluxes

Out of 25 galaxies with broad-band data 21 were measured in H α , while the remaining four were too faint to be observed through such narrow bandpasses. The total H α + [N II] fluxes of these 21 galaxies are as follows: 7 objects were found to have

fluxes consistent with zero within 1.5σ , and the others range from 1.7×10^{-14} to $7 \times 10^{-13} \text{erg/cm}^2/\text{s}$ with an average of $2.3 \times 10^{-13} \text{erg/cm}^2/\text{s}$. The $\text{H}\alpha$ -brightest galaxies (above $2 \times 10^{-13} \text{erg/cm}^2/\text{s}$) are those from the high surface brightness group. Of these, the high HI galaxies subsample seems to dominate. However, this may not be an intrinsic difference, but possibly a selection effect, with the high HI galaxies closer and larger, in general, than the low HI galaxies. These results, together with other data, are given in Table 7. Considering the $\text{H}\alpha + [\text{N II}]$ surface brightness, rather than the total line flux, the two subsamples are not markedly different from each other. The $\text{H}\alpha + [\text{N II}]$ surface brightness ranges up to $2.1 \times 10^{-15} \text{erg/cm}^2/\text{s}/\square$, with the typical value a few times smaller. Hereafter we refer to $\text{H}\alpha + [\text{N II}]$ as ‘ $\text{H}\alpha$ ’, both for convenience and, as will be discussed below, since these objects have probably relatively small contributions of nitrogen lines.

As mentioned in 3.3, the filters used have a bandpass of $\simeq 50\text{\AA}$ and the $\text{H}\alpha$ lines deviate from the central wavelength by at most 12\AA . The $\text{H}\alpha$ lines themselves have a typical width corresponding to a velocity dispersion of $\sim 180 \text{ km/s}$, i.e., $\sim 4\text{\AA}$. The combination of two profiles - the filter and the emission line makes it very difficult to correct the measured flux. We choose, therefore, not to attempt any correction, knowing that the derived fluxes may be subject to a reduction of typically 5 percent due to this effect.

Another correction that cannot be accurately derived without detailed spectroscopic information, is the contribution of the nitrogen lines to the measured $\text{H}\alpha$ line. This is mainly because galaxy lines are shifted differently relative to the peak transmission wavelength of the filters, and the $[\text{N II}]$ lines are sampled through different parts of the filters’ response curve for every galaxy. As a consequence, the $[\text{N II}]$ lines are weighted differently relative to the $\text{H}\alpha$ line for each galaxy. However, neglecting the $[\text{N II}]$ contribution will not affect our results significantly. The typical $[\text{N II}]/\text{H}\alpha$ ratio is less than 0.10 for dwarf irregulars (e.g., Kennicutt 1983, Gallagher and Hunter 1989), as in general they have lower metallicities than spirals and lenticulars. This effect is in the opposite direction to the previous one, namely, it increases the flux we assign to the $\text{H}\alpha$ line, while the effect of misalignment of the line with the filter decreases the measured flux. To our estimate, both effects are within the errors of our measurements.

A greater effect on the $\text{H}\alpha$ results is the internal dust extinction. Again, this is different from one galaxy to another, and is more difficult to account for. As in the broad-band section, we stick to the raw data as far as presentation of the results is concerned and consider this effect in a subsequent paper. This applies for both the $\text{H}\alpha$ fluxes and the equivalent widths of the lines. The $\text{H}\alpha$ equivalent widths are also shown in Table 7, together with the corresponding fluxes.

VCC no.	Group	H α flux <i>erg/cm²/s</i>	H α surface brightness <i>erg/cm²/s/□''</i>	EW(H α + [N II]) Å
144	1	$(7.05 \pm 0.76) \times 10^{-13}$	$(2.11 \pm 0.23) \times 10^{-15}$	159 ± 22
324	1	$(6.31 \pm 0.43) \times 10^{-13}$	$(6.37 \pm 0.44) \times 10^{-16}$	56 ± 4
1791	1	$(4.03 \pm 0.19) \times 10^{-13}$	$(2.21 \pm 0.11) \times 10^{-16}$	59 ± 3
459	1	$(2.97 \pm 0.33) \times 10^{-13}$	$(4.32 \pm 0.48) \times 10^{-16}$	56 ± 7
1374	1	$(2.97 \pm 0.13) \times 10^{-13}$	$(2.07 \pm 0.09) \times 10^{-16}$	49 ± 3
1725	1	$(2.42 \pm 0.29) \times 10^{-13}$	$(1.55 \pm 0.19) \times 10^{-16}$	38 ± 5
513	2	$(2.17 \pm 0.20) \times 10^{-13}$	$(4.39 \pm 0.42) \times 10^{-16}$	53 ± 5
562	2	$(1.34 \pm 0.09) \times 10^{-13}$	$(3.13 \pm 0.23) \times 10^{-16}$	84 ± 9
17	3	$(1.03 \pm 0.15) \times 10^{-13}$	$(1.06 \pm 0.16) \times 10^{-16}$	45 ± 7
10	1	$(9.3 \pm 1.9) \times 10^{-14}$	$(2.98 \pm 0.61) \times 10^{-16}$	31 ± 7
1179	2	$(6.0 \pm 2.4) \times 10^{-14}$	$(6.2 \pm 2.5) \times 10^{-17}$	20 ± 8
410	2	$(5.04 \pm 0.46) \times 10^{-14}$	$(3.42 \pm 0.31) \times 10^{-16}$	77 ± 10
985	2	$(3.1 \pm 1.8) \times 10^{-14}$	$(5.6 \pm 3.3) \times 10^{-17}$	18 ± 11
83	3	$(1.66 \pm 0.81) \times 10^{-14}$	$(2.5 \pm 1.2) \times 10^{-17}$	8 ± 4
172	1	$(3.7 \pm 6.0) \times 10^{-14}$	$(6.0 \pm 9.6) \times 10^{-17}$	8 ± 13
260	4	$(3.2 \pm 2.1) \times 10^{-14}$	$(4.5 \pm 3.1) \times 10^{-17}$	128 ± 104
2033	2	$(2.1 \pm 1.5) \times 10^{-14}$	$(1.5 \pm 1.1) \times 10^{-17}$	5 ± 3
24	1	$(1.5 \pm 4.9) \times 10^{-14}$	$(0.4 \pm 1.4) \times 10^{-16}$	6 ± 20
1013	4	$(8.1 \pm 7.6) \times 10^{-15}$	$(2.2 \pm 2.1) \times 10^{-17}$	10 ± 10
22	2	$(0.5 \pm 2.0) \times 10^{-14}$	$(1.4 \pm 5.0) \times 10^{-17}$	4 ± 13
168	4	$(-6.2 \pm 4.9) \times 10^{-15}$		

Table 7: H α data in decreasing order of H α line flux. The galaxies in the lower panel have values consistent with zero within 1.5σ .

5.3 Combined results

The UV monochromatic magnitudes obtained from the IUE observations or from FAUST were combined with the optical monochromatic magnitudes from the Wise Observatory to yield a rough spectral energy distribution of the sample galaxies. No correction for internal extinction was made. Unfortunately, only 6 galaxies were detected in the UV. Nine other galaxies have UV upper limits from FAUST images and nine others have no UV data at all. The galaxies with UV magnitudes are plotted in Figure 5, the galaxies with upper limits in Figure 6, and the ones with no UV data in Figure 7.

As expected from the broad-band data, the SEDs of the galaxies display a variety of behaviors. In Figure 5, three of the galaxies have steep SEDs (two were detected by FAUST and VCC144 was chosen for observation by IUE due to its strong H α emission), and three have flat SEDs. It should be noted that for galaxies with IUE data only the SED of the inner part of the galaxy is plotted, as explained in 4.3.1.

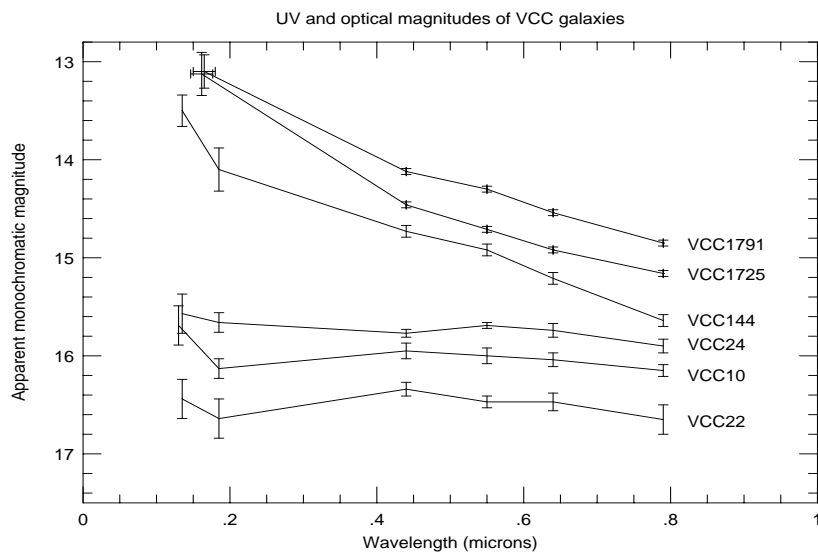


Figure 5: Spectral energy distribution of sample galaxies with UV data. The UV points of VCC10 and VCC1725 are slightly shifted for clarity.

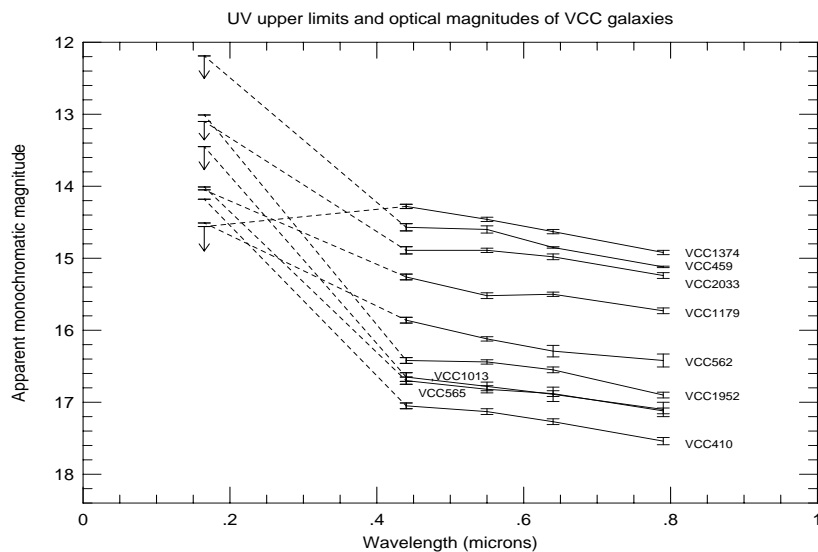


Figure 6: Spectral energy distribution of sample galaxies which have upper limits for UV radiation. For clarity, not all upper limit arrows are shown.

6 Discussion

An interesting relation is apparent between the V magnitude and the recession velocity of the galaxies, as derived from the HI line (Figure 8). There is a general negative correlation between the two parameters. The point in the upper right corner of the plot is VCC806, a very faint object barely detected in the radio and optical, which

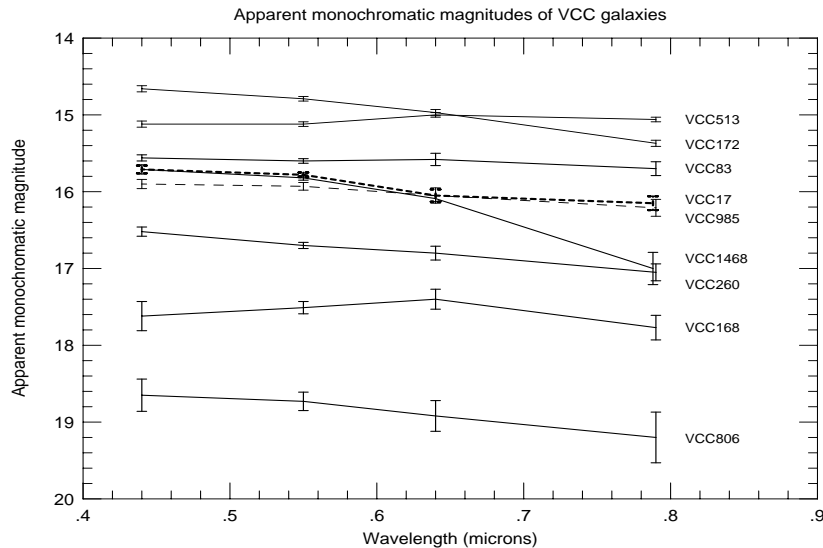


Figure 7: Spectral energy distribution of sample galaxies with no UV data.

may be a background galaxy. If we exclude this point, the correlation coefficient is -0.55 . The correlation coefficient between the recession velocity and the V-band fluxes of the galaxies corresponding to their magnitudes is 0.46 .

This correlation may lead to the following empirical conclusion: if faint galaxies in Virgo are characterized by lower recession velocities, a Malmquist bias will cause the depletion of slowly receding galaxies in the sample. This may explain the observed skewness of the velocity distribution of faint dwarfs in Virgo (Binggeli *et al.* 1993). These velocities are shifted, in general, towards higher values, compared with the velocity distribution of other galactic types. We may expect, therefore, that many faint dwarf galaxies which do not yet have velocity data are mostly slowly receding, with velocities in the range of $0\text{--}1500$ km/s. This may balance the skewness of the velocity distribution of these galaxies.

As for the origin of this correlation, it may arise because of infall of galaxies towards the Virgo cluster core (e.g., Tully and Shaya 1984, Binggeli *et al.* 1993). Galaxies which are between us and the core appear brighter and are falling away from the observer to the cluster core, while galaxies behind the core are falling ‘toward’ us, having a recession velocity lower than that of the core itself (around 1200 km/s). This would produce the effect of negative correlation seen here and, according to this interpretation, the faint Virgo dwarfs lacking velocity data would be those behind the cluster core. It should be noted, however, that this effect, in its simple interpretation, does not match the data perfectly. This is because the range of magnitudes of the sample galaxies, which is correlated to the recession velocity, is roughly $1.5\text{--}3$ mag, depends on the intrinsic scatter of absolute magnitudes assumed for the sample. This range corresponds to a difference in distance of a factor of $2\text{--}4$ between the near

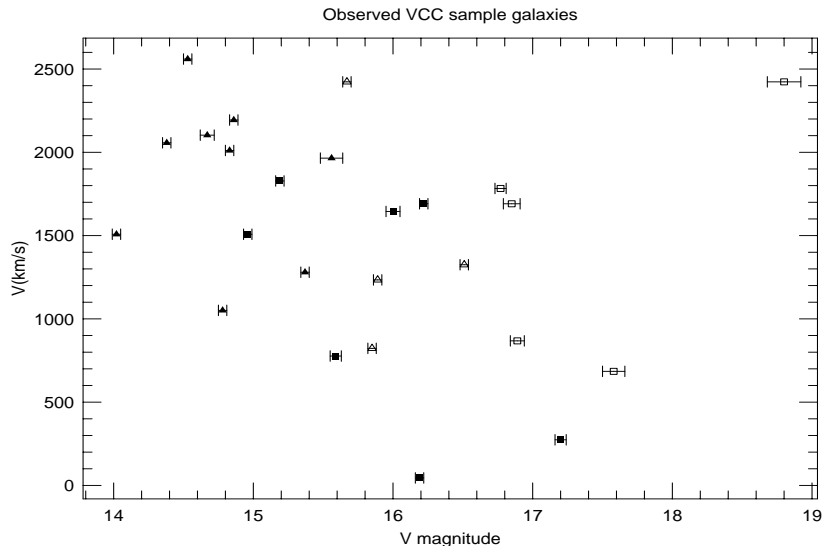


Figure 8: Recession velocities of the sample galaxies versus the observed magnitude. The negative slope may indicate infall of the galaxies into the cluster core (see text).

and far galaxies of the sample, which is not likely to be the case in Virgo.

The broad-band B–V colors of the sample galaxies are relatively blue, ranging from ~ 0.42 to ~ 0.72 . Unlike our previous assumption presented in section 2, no correlation between B–V and the optical surface brightness was found. The scatter in the B–V results indicates that the galaxies do not share the same properties. This is better demonstrated in the color-color diagram of V–R vs. R–I [Figure 9a]. In this diagram, the points are further dispersed due to the variation of H α equivalent widths of the galaxies. The H α line is included in the broad R band and may change the total R flux of strong-emission-line galaxies. For this reason, the scatter is smaller in the B–V vs. V–I diagram, which is shown in Figure 9b. However, note that in the galaxy with the most intense H α (VCC144), the contribution of the H α line to the broad-band R is less than 15%. Another reason for the scatter may be different amounts of internal extinction in each galaxy, which may arbitrarily shift the galaxy on the diagram, albeit in the general direction of the color-color dependence.

In Figures 9a and 9b the galaxies with high HI content are marked by triangles and those with low HI content by squares. High surface brightness galaxies are marked by filled symbols and low surface brightness ones by empty symbols. There are clearly not enough low surface brightness objects for meaningful statistical conclusions, but the high surface brightness group shows a difference between the high HI content (filled triangles) and the low HI content (filled squares). They share the same range of B–V color index but the lower HI group seems to have redder V–R color. The sample should be enlarged before clearer conclusions can be drawn about this effect.

The measured H α equivalent widths of the galaxies are relatively high, typically $\sim 50\text{\AA}$, and up to 159\AA . Again, the high surface brightness sub-samples have higher

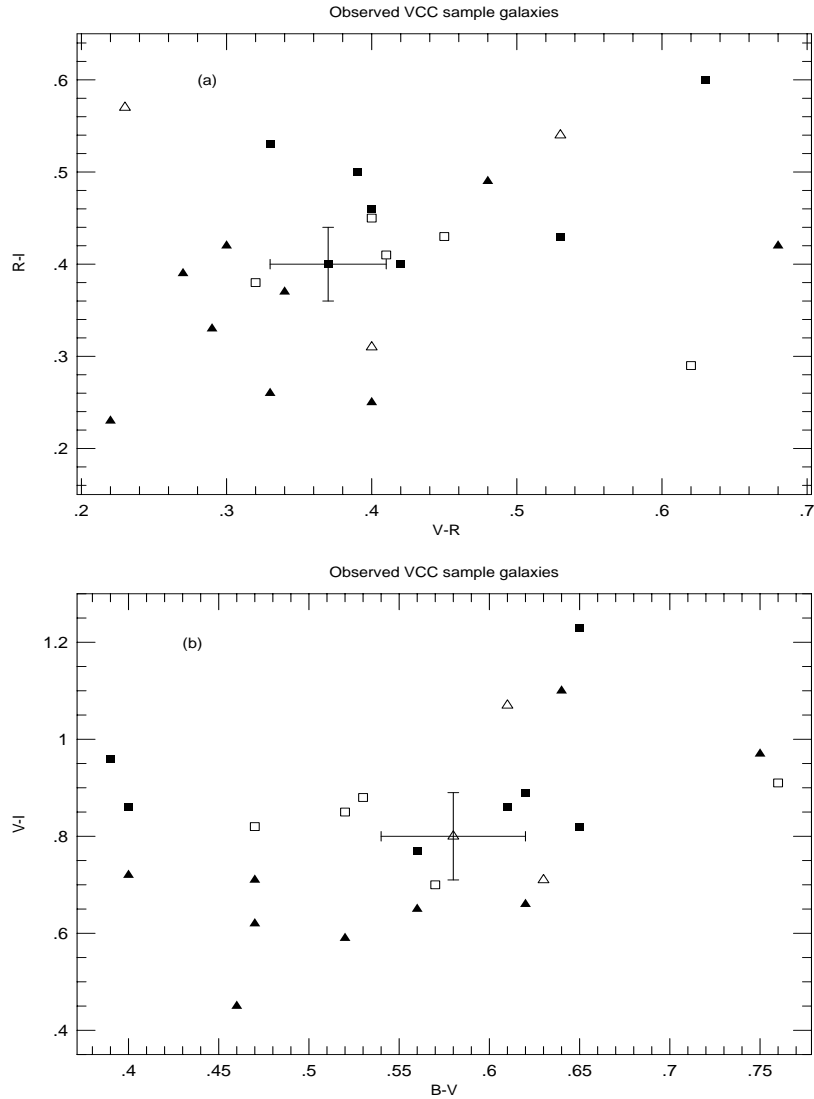


Figure 9: Color-color diagrams of the sample galaxies. In (a) the R band increases the dispersion of the objects. In (b) this band is not included and the dispersion is smaller. The galaxies with high HI content are marked by triangles and those with low HI content by squares. High surface brightness galaxies are marked by filled symbols and the low surface brightness ones by empty symbols. A typical error bar is displayed with one of the points in each diagram.

$EW[H\alpha]$ than others. This implies that a large fraction of the surface of the galaxies is covered by one or more HII regions. Some BCD galaxies are also known as extragalactic HII regions or HII galaxies. This name is very suitable for some of the sample galaxies. In the case of VCC144, where the equivalent width is 159\AA , the entire galaxy is one giant HII region.

The high $H\alpha$ flux and $EW[H\alpha]$, together with the spatial appearance of the sample galaxies in $H\alpha$, namely the fraction of galactic surface covered by HII regions,

emphasize the high SFR of some of the galaxies, and the starburst activity that takes place in them. On the other hand, other galaxies in the sample show little or no H α emission, which indicates their low current star formation activity. There appears to be no correlation between the H α flux and the HI 21cm line flux.

7 Conclusion

We presented observations related to star formation properties of a sample of late-type dwarf galaxies. The intention in focusing on dwarf galaxies was to exclude some of the star formation inducing mechanisms, assumed to account for star formation in large galaxies. In addition, we concentrate on Virgo cluster members, in order to test the effects of the cluster environment on the star formation properties of the galaxies.

A data base consisting of a number of broad-band colors and H α line observations is important for determining the ongoing star formation process, as well as the star formation history of the sample. In a subsequent paper we will show that some of the galaxies show signs of a strong burst of star formation, while others completely lack signs of recent star formation activity.

The observational data are affected primarily by internal dust extinction in the galaxies, which complicates the interpretation of the data. This effect will be discussed in detail in the next paper.

Another interesting finding, concerning the dwarf galaxies in Virgo, is their velocity field. Our results indicate an infall of the galaxies towards the cluster core (see 5.1). We suggest that this explains partly the skewed recession velocity distribution of the dwarf galaxies, in terms of a Malmquist bias.

Acknowledgments

Observations at the Wise Observatory are partly supported by a Center of Excellence Grant from the Israel Academy of Sciences. UV studies at the Wise Observatory are supported by special grants from the Ministry of Science and Arts, through the Israel Space Agency, to develop TAUVEEX, a UV space imaging experiment, and by the Austrian Friends of Tel Aviv University.

EA was supported partly by a grant from "The Fund for the Encouragement of Research" Histadrut- The General federation of Labour in Israel. NB acknowledges the hospitality of Prab Gondhalekar and of the IRAS Postmission Analysis Group at RAL, as well as IRAS Faint Source catalog searches by Rob Assendorp.

We thank Stuart Bowyer and Tim Sasseen from the Space Sciences Laboratory, Berkeley, University of California, for kindly providing the FAUST images of the Virgo cluster.

References

- Allen, C.W. 1973, *Astrophysical Quantities*, The Athlone Press, University of London.
- Almoznino, E., Loinger, F. & Brosch, N. 1993, Mon. Not. R. astr. Soc. **265**, 641.
- Bianchi, L., Northover, K. & Clavel, J. 1981, *IUE VILSPA USERS GUIDE*, volume II - *Image Processing*.
- Binggeli, B., Sandage, A. & Tammann, G.A. 1985, Astron.J. **90**, 1681 (BST).
- Binggeli, B., Popescu, C.C. & Tammann, G.A. 1993, Astron. Astrophys. Suppl. **98**, 275.
- Bowyer, S., Sasseen, T.P., Wu, X. & Lampton, M. 1995, Astrophys. J. Suppl. **96**, 461.
- Brosch, N., Almoznino, E., Leibowitz, E.M., Netzer, H., Sasseen, T.P., Bowyer, S., Lampton, M. & Wu, X. 1995, Astrophys. J. **450**, 137.
- Brosch, N., Almoznino, E., & Hoffman, L. 1996, preprint.
- Brosch, N., Formiggini, L., Almoznino, E., Sasseen, T.P., Lampton, M. & Bowyer, S. 1996, preprint.
- Bruzual, G.A., & Charlot, S. 1993, Astrophys. J. **405**, 538 (BC93).
- Buat, V., Deharveng, J.M. & Donas, J. 1989, Astron. Astrophys. **223**, 42.
- Calzetti, D., Kinney, A.L. & Storchi-Bergmann, T. 1994, Astrophys. J. **429**, 582.
- de Vaucouleurs, G., de Vaucouleurs, A., Corwin, H.G. Buta, R.J., Paturel, G. & Fouqué, P. 1991, *The Third Reference Catalog of Bright Galaxies*, (Springer, New-York).
- Drinkwater, M. & Hardy, E. 1991, Astron.J. **101**, 94.
- Fernie, J.D. 1983, PASP **95**, 782.
- Fouqué, P., Bottinelli, L., Gouguenheim, L. & Paturel, G. 1990, Astrophys. J. **349**, 1.
- Gallagher, J.S., Hunter, D.A. & Tutukov, A.V. 1984, Astrophys. J. **284**, 544 (GHT).
- Gallagher, J.S. & Hunter, D.A. 1986, Astron.J. **92**, 557.
- Gallagher, J.S. & Hunter, D.A. 1989, Astron.J. **98**, 806 (GH89).

- Gondhalekar, P.M., Morgan, D.H., Dopita, M. & Phillips, A.P. 1984, Mon. Not. R. astr. Soc. **209**, 59.
- Haynes, M.P., Herter, T., Barton, A.S. & Benensohn, J.S. 1990, Astron.J. **99**, 1740.
- Hoffman, G.L., Helou, G., Salpeter, E.E., Glosson, J. & Sandage, A. 1987, Astrophys. J. Suppl. **63**, 247.
- Hoffman, G.L., Williams, H.L., Salpeter, E.E., Sandage, A. & Binggeli, B. 1989, Astrophys. J. Suppl. **71**, 701.
- Hunter, D.A. & Gallagher, J.S. 1985, Astron. Astrophys. Suppl. **58**, 533.
- Kennicutt, R.C. 1983, Astrophys. J. **272**, 54 (K83).
- Kennicutt, R.C. & Kent, S.M. 1983, Astrophys. J. **88**, 1094.
- Kennicutt, R.C. 1989, *Large Scale Star Formation & the Interstellar Medium*, in "The Interstellar Medium in External Galaxies". ed. H.A.Thronson & J.M.Shull.
- Kennicutt, R.C., Tamblyn, P. & Congdon, C.W. 1994, Astrophys. J. in press. Also Steward Observatory preprint no. 1194.
- Kunth, D. & Sargent, W.L.W. 1986, Astrophys. J. **300**, 496.
- Landolt, A.U. 1973, Astron.J. **78**, 958.
- Landolt, A.U. 1992, Astron.J. **104**, 340.
- Larson, R.B. 1986, Mon. Not. R. astr. Soc. **218**, 409.
- Larson, R.B. 1987, *Star Formation Rates & Starbursts*, in "Starbursts & Galaxy Evolution". ed. T.X.Thuan, T.Montmerle & J.T.T.Van (Edition Frontieres, Gif sur Yvette - FRANCE).
- Mas-Hesse, J.M. & Kunth, D. 1991, Astron. Astrophys. Suppl. **88**, 399.
- Massey, P., Strobel, K., Barnes, J.V. & Anderson, E. 1988, Astrophys. J. **328**, 315.
- Miller, G.E. & Scalo, J.M. 1979, Astrophys. J. Suppl. **41**, 513 (MS79).
- Osterbrock, D.E. 1989, *Astrophysics of Gaseous Nebulae & Active Galactic Nuclei*, (Mill Valley, CA: University Science Books).
- Pogge, R.W. & Eskridge, P.B. 1987, Astrophys. J. **93**, 291 (PE87).
- Pogge, R.W., Goodrich, R.W. & Veilleux, S. 1988, *The VISTA Cookbook*, Lick Observatory Technical Report No. 50, University of California, CA.

- Salpeter, E.E. 1955, *Astrophys. J.* **121**, 161 (S55).
- Sandage, A. 1986, *Astron. Astrophys.* **161**, 89.
- Savage, B.D. & Mathis, J.S. 1979, *Ann. Rev. Astron. Astrophys.* (SM).
- Scalo, J.M. 1986, *Fundamentals of Cosmic Physics* **11**, 1 (S86).
- Scalo, J.M. 1987, *The Initial Mass Function, Starbursts and the Milky Way*, in "Starbursts and Galaxy Evolution". ed. T.X.Thuan, T.Montmerle & J.T.T.Van (Edition Frontieres, Gif sur Yvette - FRANCE).
- Schmidt, M. 1959, *Astrophys. J.* **129**, 243.
- Shemi, A., Mersov, G., Brosch, N. & Almozino, E. 1993, *The Prediction of Stellar Ultraviolet Colours*, in "Astronomical Data Analysis Software and Systems III", ed. Crabtree, D.R., Hamisch, R.J. and Barnes, J. (A.S.P. conference series, Volume 61).
- Shields, G.A. 1990, *Ann. Rev. Astron. Astrophys.* **28**, 525.
- Terlevich, R. & Melnick, J. 1983, ESO preprint no. 264.
- Thronson, H.A. & Telesco, C.M. 1986, *Astrophys. J.* **311**, 98.
- Tully, R.B. & Shaya, E.J. 1984, *Astrophys. J.* **281**, 31.
- van der Hulst, J.M., Kennicutt, R.C., Crane, P.C. & Rots, A.H. 1988, *Astron. Astrophys.* **195**, 38.
- Young, J.S. & Knezek, P.M. 1989, *Astrophys. J. Lett.* **347**, L55.